Chemical Science

ROYAL SOCIETY OF CHEMISTRY

EDGE ARTICLE

View Article Online
View Journal

Cite this: DOI: 10.1039/d5sc08871b

All publication charges for this article have been paid for by the Royal Society of Chemistry

Zero-trigger ultrafast charge-transfer J-aggregates *via* Se/π-directed assembly enable synchronous ROS/heat amplification for NIR-II photoimmunotherapy

Dandan Ma,†[a] Hui Bian, †[b] Fei Pan, [c] Danhong Zhou, [d] Zhi Chen, [e] Haoying Ge,[d] Yuanlang Guo,[a] Yingnan Wu,[a] Xin He, [a] Panwang Zhou, [f] Lei Wang, [a] Xiaoqiang Chen*[a] and Xiaojun Peng *[ad]

Supramolecular J-aggregation of π-conjugated photosensitizers provides a powerful strategy to optimize phototheranostic performance. However, integrating facile assembly with photodynamic and photothermal (PDT/PTT) synergy remains challenging. Herein, we report a charge transfer (CT)-state J-aggregation paradigm using a selenium-embedded molecular framework (**FUC-Se**). Driven by directional π−π stacking and Se···Se interactions, **FUC-Se** undergoes ultrafast (<5 s) self-assembly in water, forming stable CT-J aggregates without external triggers. Moreover, these aggregates enable concurrent amplification of reactive oxygen generation (Φ_Δ = 0.139, 6 × monomer) and photothermal conversion (η = 47.69%, 13× monomer) through (i) reducing the singlet-triplet energy gap by 57% (ΔE_{S1T1} = 0.25 eV *vs.* 0.58 eV) and enhancing spin–orbit coupling 9-fold (7.14 cm^{-1} *vs.* 0.78 cm^{-1}); (ii) promoting non-radiative decay with 77% surge in geometry reorganization ($RMSD_{S1\rightarrow S0}$ = 0.209 *vs.* 0.118) and 127% increase in the Huang–Rhys factor (λ_h = 0.25 eV *vs.* 0.11 eV). Phospholipid remodeling yields tumor-targeted **FUC-Se@LP** with hypoxia-tolerant ROS/PTT and NIR-II imaging. **FUC-Se@LP** achieves NIR-II-guided PDT/PTT, eradicating hypoxic tumors (IC_{50} = 2.47 μM) and suppressing metastasis *via* immunogenic cell death. This work establishes the first CT-J aggregate unifying exogenous-trigger-free ultrafast self-assembly, NIR-II imaging, and dual PDT/PTT enhancement, providing a promising strategy for precision oncology.

Received 13th November 2025
Accepted 14th February 2026

DOI: 10.1039/d5sc08871b

rsc.li/chemical-science

Introduction

Phototherapy, which spatiotemporally channels photon energy into cytotoxic signals, including reactive oxygen species (ROS) in photodynamic therapy (PDT) and localized hyperthermia in photothermal therapy (PTT), has significantly advanced oncotherapy.[1–7] Despite significant anticancer advances, clinical translation remains hindered by intrinsic limitations of conventional π-conjugated photosensitizers (PSs), such as weak near-infrared absorption compromising tissue penetration, aggregation-caused quenching (ACQ) from uncontrolled stacking, and nonspecific biodistribution reducing tumor targeting efficiency.

Supramolecular J-aggregation of π-conjugated PSs offers a promising strategy to modulate their optical properties and biodistribution profiles, endowing them with unique capabilities to address these challenges.[8–16] Specifically, (i) redshifted absorption/emission *via* J-type exciton coupling enables deeper NIR photon penetration;[17–23] (ii) enhanced extinction coefficients and exciton–exciton annihilation promote photothermal conversion;[24–29] (iii) certain J-aggregate architectures may reduce singlet–triplet energy gaps (ΔE_{ST}), potentially enhancing intersystem crossing (ISC) for ROS generation;[30–33] (iv) morphology-dependent biological behaviors (*e.g.*, circulation time, cellular uptake, and organ distribution) can be tuned by stacking modes.[34–36] Collectively, these advances position J-aggregation as a transformative platform to overcome the penetration–quenching–targeting trilemma of conventional PSs.

[a]*College of Materials Science and Engineering, Shenzhen University, Shenzhen 518060, P.R. China. E-mail: chenxq@szu.edu.cn; pengxj@dlut.edu.cn*

[b]*Department of Chemistry and Nanoscience, Ewha Womans University, 03760 Seoul, Republic of Korea*

[c]*Institute of Apicultural Research, Chinese Academy of Ag-ricultural Sciences, Beijing 100093, P. R. China*

[d]*State Key Laboratory of Fine Chemicals, Frontiers Science Center for Smart Materials, Dalian University of Technology, Dalian, 116024, P.R. China*

[e]*College of Chemistry and Environmental Engineering, Shenzhen University, Shenzhen, Guangdong 518060, P.R. China*

[f]*State Key Laboratory of Catalysis, National Laboratory for Clean Energy, Dalian Institute of Chemical Physics, Chinese Academy of Sciences, Dalian, 116023, P.R. China*

† These authors contributed equally.

However, most existing J-aggregate phototheranostics rely on cumbersome assembly protocols, such as specific solvent,[37–39] precise thermal[40–43]/ionic control,[44–46] or carrier assistance[47–56] for stable nanostructure formation. This complexity not only risks dissociation under physiological conditions (*e.g.*, hemodilution-induced disassembly, thermal reversion at 37 °C, RES clearance) but also conflicts with clinical demands for simplified formulations. In this context, the concept of zero-trigger or exogenous-trigger-free assembly, where the aqueous environment itself serves as the sole thermodynamic driver without requiring any additional stimuli, becomes highly desirable yet remains largely unmet. Critically, most J-aggregates function exclusively as either PDT or PTT agents. Even the mere three reported J-aggregate systems demonstrating concurrent PDT/PTT effects fundamentally rely on exogenous stabilization methods, including solvent-triggered aggregation,[57] sonication-induced crystallization,[58] and surfactant-mediated phase transitions.[37] Thus, the persistent failure of this field to achieve rapid, modulator-free aqueous J-aggregation with dual ROS/heat amplification constitutes a critical translational barrier.

Herein, we pioneer a selenium-directed charge-transfer J-aggregation paradigm through rational substitution of indole with selenazole in the well-established Changsha dye scaffold (Lin *et al.*, 2012).[59] The engineered **FUC-Se** intrinsically generates synergistic supramolecular forces, including cooperative π–π stacking (3.7 Å) and directional Se···Se contacts (4.0 Å), both of which contributed to drive exogenous-free, ultrafast (<5 s) J-aggregation in aqueous media. Crucially, unlike conventional J-aggregates limited to bathochromic shifts, the resulting CT-J architecture establishes interfacial charge-transfer states that reconfigure excited energy landscapes. This unique electronic reconstruction synergistically enhances intersystem crossing (ISC) while promoting vibronic thermalization, enabling concurrent amplification of singlet oxygen (Φ_Δ = 0.139, 6 × monomer) and heat conversion (η = 47.69%, 13 × monomer) (Scheme 1a). Subsequent phospholipid remodeling further transforms the insoluble sheets into tumor-targeted

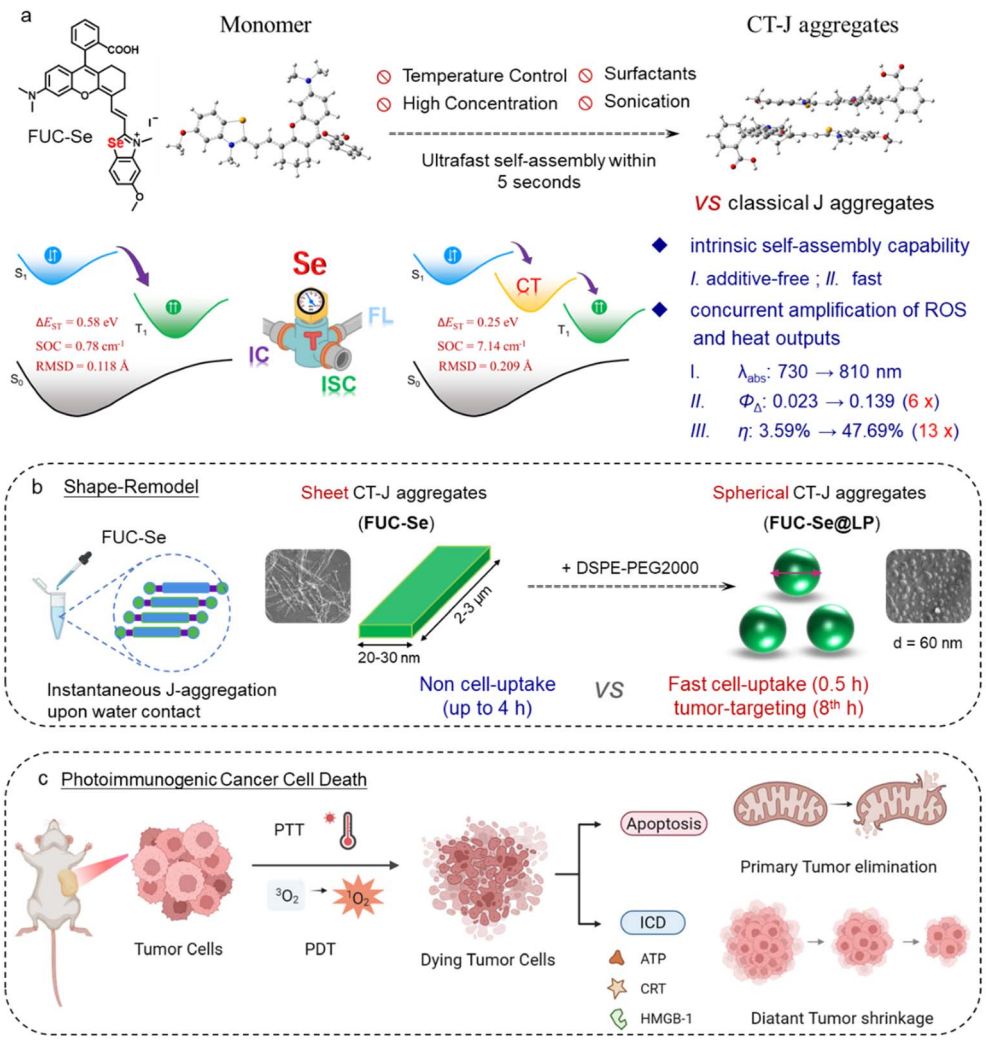

Scheme 1 (a) Photophysical mechanism and remarkable phototheranostic performance of **FUC-Se** CT-J aggregates (**FUC-Se@LP**). (b) Phospholipid-assisted morphological evolution from sheet to spherical CT-J aggregates. (c) Photoimmunogenic cancer cell death induced by **FUC-Se@LP**.

nanospheres (**FUC-Se@LP**), which exhibit rapid cellular uptake (complete within 30 min), peak tumor accumulation at 8 h post-injection, dual hypoxia-tolerant ROS generation (Type I/II), and NIR-II imaging capability (Scheme 1b). Under NIR-II fluorescence guidance, **FUC-Se@LP** eradicates primary tumors while triggering immunogenic cell death *via* DAMP release, systemically inhibiting non-irradiated distant metastases (Scheme 1c). Overall, our J-aggregate system presents a promising strategy for solid tumor management by integrating three significant advantages, including facile and rapid assembly enabling off-the-shelf formulation, hypoxia-defying dual-mode therapy overcoming tumor resistance and phototherapy-initiated systemic immunity suppressing distant lesions. A quantitative comparison of key parameters between our system and other state-of-the-art J-aggregates[60–62] is summarized in Table S1, highlighting the integrated advantages of our CT-J platform.

Results and discussion

Molecular design

Hemicyanine dyes, characterized by a donor–π–acceptor (D–π–A) architecture, provide a versatile molecular platform for tailoring phototherapeutic and self-assembly properties through structural modularity.[63–65] A landmark advancement came with Lin *et al.*'s rhodamine–hemicyanine hybrids (termed Changsha dyes CS1-6), comprising a rhodamine derivative and an indole/benzoindole segment connected by a vinyl bridge. This fusion synergizes the advantages of both parent dyes, NIR absorption/emission coupled with rhodamine-like fluorescence switching behavior, which cemented its status as a privileged and widely exploited framework in dye chemistry. Plenty of derivatization strategies, including carboxylic-acid-controlled spirocyclization, π-extension, and heterocycle replacement, have expanded this scaffold for bioimaging, sensing and diagnostics.[66–72] Yet, despite these functional developments, the fundamental aggregation and assembly behavior of this hybrid skeleton remains largely unexplored. To transform this inert scaffold into a potent J-aggregation platform, we herein rationally replace indole with selenazole based on three design considerations: (i) Se's heavy-atom effect will boost ISC for ROS amplification;[73,74] (ii) selenazole's intrinsic planar rigidity (*vs.* indole) will redshift absorption and facilitate ordered π-stacking; (iii) directional Se···Se interactions, well proven to facilitate interchain charge transfer in polymer photovoltaics,[75–78] may induce and stabilize charge-separated states while acting as structural "zippers" to cooperatively guide π–π stacking toward ordered architectures. Thus, we speculate that such a transformation will simultaneously promote photosensitization and directional assembly arrangement. To validate this design, we synthesized **FUC-N** (indole-based control) and **FUC-Se** (selenazole-engineered analog). The

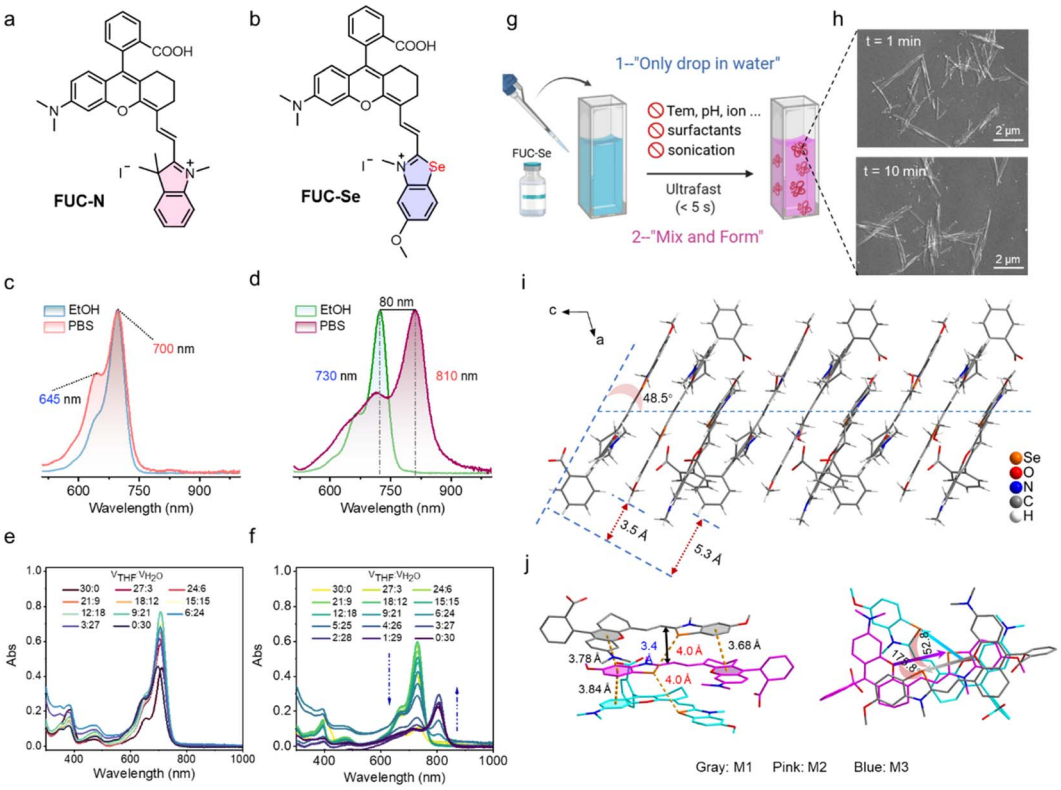

Fig. 1 Chemical structures of (a) **FUC-N** and (b) **FUC-Se**, respectively. Normalized absorption spectra of (c) **FUC-N** and (d) **FUC-Se** in ethanol and PBS, respectively. Absorption spectra of (e) **FUC-N** and (f) **FUC-Se** in THF–water mixtures with different volume ratios, respectively. (g) Schematic diagram of the preparation process of FUC-Se J aggregates. (h) SEM images of **FUC-Se** J-aggregates prepared at different times. Single-crystal packing structure of **FUC-Se** (i) with a slippage angle (θ_{qui} = 48.5°) and (j) π–π interaction distance ($d_{\pi-\pi}$ = 3.4 Å) and Se···Se van der Waals distance (d_{Se-Se} = 4.0 Å).

detailed synthesis routes and structural characterization are shown in the SI (Fig. S21–S24).

Optical properties

UV-Vis-NIR absorption spectra reveal that both dyes exhibit strong π–π* transitions with high extinction coefficients (>10^5 L mol^{-1} cm^{-1}) in organic solvents (Fig. S1 and Table S2). And, **FUC-Se** displays a 30 nm redshift in absorption maxima (λ_{abs} = 730 nm) relative to **FUC-N** (λ_{abs} = 700 nm) due to larger planar rigidity of selenazole. Strikingly, they exhibited distinct spectral behaviors in PBS. **FUC-N** maintains its monomeric profile in PBS *versus* ethanol at concentrations up to 20 μM (Fig. 1c and S2a), whereas **FUC-Se** exhibits a pronounced red shift in water with λ_{abs} shifting from 730 to 810 nm, even at a dramatically lower concentration of 1 μM (Fig. 1d and S1–S2b). To exclude the effect of water polarity on the wavelength redshift, the absorption spectra in the THF/water binary system with varying water fractions (f_w) were recorded. As shown in Fig. 1e, **FUC-N** exhibits only minor intensity fluctuations at 700 nm without peak displacement across all f_w. Conversely, **FUC-Se** shows f_w-dependent spectral evolution (Fig. 1f). Specifically, it maintained monomeric character (λ_{abs} = 730 nm) when f_w < 80%, but exhibited a fixed 810 nm band at f_w = 80%, which progressively intensified with increasing water (Fig. 1f). Moreover, similar spectral evolution was observed in EtOH/water and DMSO/water mixtures (Fig. S3), confirming that this aggregation behavior is independent of organic solvent identity. The combination of (i) fixed-wavelength redshift, (ii) threshold concentration dependence, and (iii) intensity growth of the new band provides solid evidence for J-aggregation of **FUC-Se** in water. Collectively, selenazole substitution successfully converts the inert scaffold into a J-aggregation platform, validating our molecular design.

Notably, **FUC-Se** accomplishes spontaneous, ultra-fast and exogenous-trigger-free J-aggregation in aqueous media. This is rarely achieved in prior phototheranostic J-aggregates. Merely dispersing a 1 μM solution into water with brief pipette mixing (<5 s) immediately generates a characteristic J-aggregate absorption band at 810 nm (Fig. 1g and S2). Critically, this "mix-and-form" transition proceeds identically in both ultrapure water and PBS (Fig. 1d and S3) without any external triggers (temperature, pH, ultrasound, or surfactants). Scanning electron microscopy (SEM) confirms rapid nanostructure formation. The well-defined nanosheets with uniform dimensions (1–2 μm × 20–30 nm) emerge within 1 minute and maintain morphological integrity after 10 minutes (Fig. 1h). Atomic force microscopy (AFM) further confirmed the sheet-like morphology of the aggregates (Fig. S4). This combination of techniques confirms that barrierless molecular assembly generates macroscopic, two-dimensional architectures.

X-ray single-crystal structure analysis

The single-crystal structure unequivocally demonstrates that **FUC-Se**'s remarkable J-aggregation stems from a hierarchically organized assembly process driven by π–π stacking and

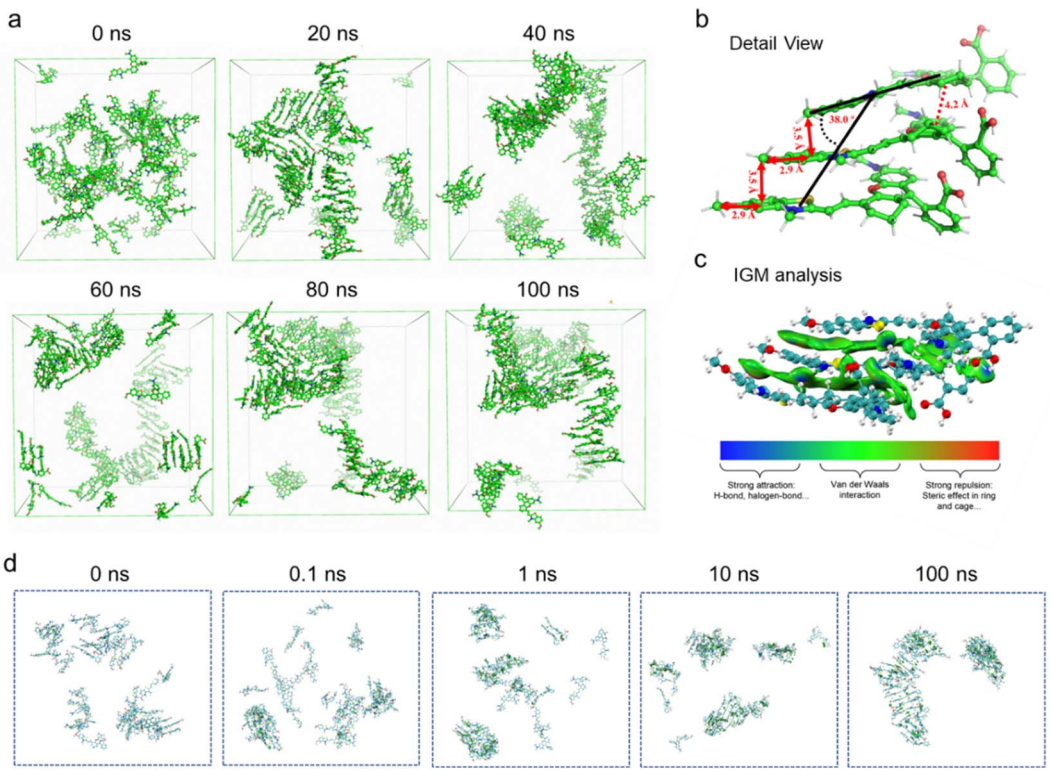

Fig. 2 (a) Trajectories of self-assembled systems of **FUC-Se**. (b) Detailed view of **FUC-Se** J-aggregates formed in pure water. (c) IGM plot isosurface for **FUC-Se** J-aggregates from (b) (100 ns). Blue represents attractive or bonding interactions, green represents weak van der Waals interactions, and more green-colored atoms contribute more to the interaction, while red represents repulsive interactions. (d) Spatiotemporal visualization of driving forces in **FUC-Se** aggregation.

directional Se···Se bonding, orchestrated by precise molecular rotations (Fig. 1i–j and Tables S3–S4). In the asymmetric unit, there are three **FUC-Se** molecules (marked in gray, M1; pink, M2; and blue, M3). M2 undergoes a near-perfect 178° rotation relative to M1, enabling two face-to-face π–π interactions (3.68 Å and 3.78 Å). Concurrently, a directional Se···Se chalcogen bond (4.0 Å) bridges M1 and M2. This interaction acts as a "structural clamp", rigidly fixing the 178° orientation and slip distance (3.5 Å). This corroborates our initial rationale that Se···Se contacts would act as "structural zippers" to cooperatively guide the assembly process. This M1–M2 dimer constitutes the fundamental excitonic unit, which is the primary structural basis for the large 80 nm J-band redshift (810 nm). M3 adopts a 58° rotation relative to M1, creating an asymmetric extension point. The tilted Se···Se bond enables the extension of the J-aggregate structure with controlled geometry. The cooperative interplay of Se···Se and π–π interactions, directed by specific molecular rotations, establishes the structural foundation for the rapid, exogenous-trigger-free J-aggregation of **FUC-Se** in aqueous media.

Molecular dynamics simulation insights

To further unravel the ultrafast assembly mechanism, molecular dynamics (MD) simulations were conducted using GROMACS 19.5 under periodic boundary conditions to model an infinite solution environment. As shown in Fig. 2a and Video S1, hydrophobic forces and directional Se···Se interactions initiate molecular clustering within 20 ns. Subsequent dominant π–π coupling drives rapid, oriented alignment, yielding stable J-aggregates by 100 ns with characteristic geometry, including 3.5 Å intermolecular spacing, 2.9 Å slide displacement, and slip angle 38.5° < 54.7° inclination (Fig. 2b). These parameters quantitatively match experimental crystal data (Fig. 1i and j). Complementary independent gradient model (IGM) analysis confirms π–π stacking (blue isosurfaces) as the primary driving force, with van der Waals (green) and hydrophobic interactions enabling long-range order (Fig. 2c and d). This synergy of chalcogen bonding initiation and π–π interaction rationalizes the sub-minute barrierless assembly observed experimentally.

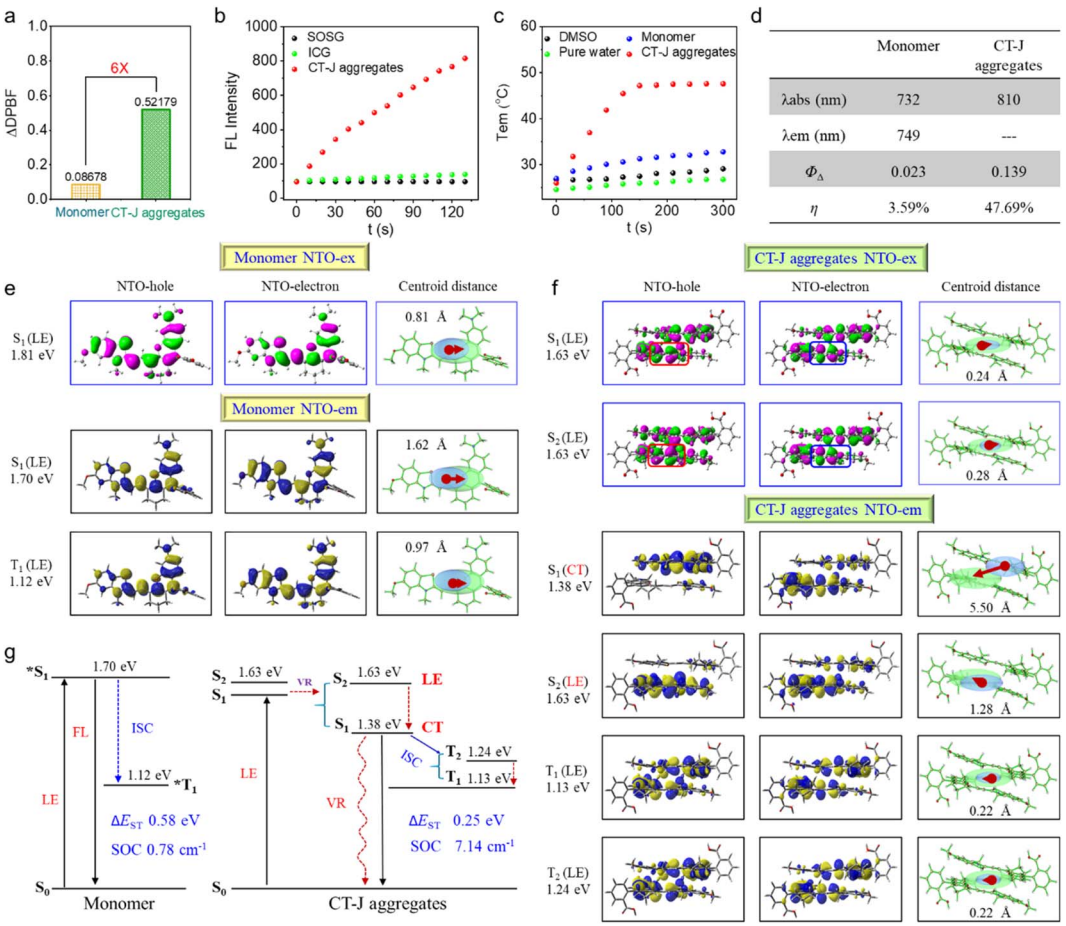

Fig. 3 Synergistic ROS/Heat dual-effect enhancement with mechanistic insights from DFT. (a) Comparison of singlet oxygen generation capacity between **FUC-Se** monomer and J-aggregates, monitored by recording absorbance changes of DPBF at 415 nm. (b) Comparison of singlet oxygen generation between **FUC-Se** J-aggregates and ICG, assessed by fluorescence changes of SOSG at 524 nm. (c) Evaluation of photothermal properties of **FUC-Se** monomer in DMSO and J-aggregates in pure water, determined by recording solution temperature changes upon light irradiation. All samples were adjusted to identical absorbance and irradiated under the same laser power density. (d) Comparison of key photophysical parameters between **FUC-Se** monomer and J-aggregates. Calculated natural transition orbital (NTO) diagrams for the ground and excited states of (e) **FUC-Se** monomer and (f) **FUC-Se** J-aggregates. (g) Jablonski diagram for both the **FUC-Se** monomer and J-aggregates.

In vitro singlet oxygen and heat generation

To quantify J-aggregation effects on photodynamic and photothermal performance, we compared singlet oxygen ($^1O_2$) generation and photothermal conversion between **FUC-Se** monomers and J-aggregates under strictly controlled identical conditions (solvent, absorption intensity, and irradiation parameters). Using DPBF as an $^1O_2$ trap, J-aggregates induced sixfold greater DPBF degradation ($\Delta_{abs} = 0.52$) than monomers within 7 min under 808 nm irradiation (Fig. 3a), a trend conserved across other solvent systems (Fig. S5). This significant enhancement was further validated using an alternative $^1O_2$ detection method based on ABDA decomposition (Fig. S6), which yielded consistent results. Using ICG as a reference ($\Phi_\Delta = 0.008$ in water),[79,80] complementary SOSG assays further quantified Φ_Δ of J-aggregates (0.139), 6× higher than that of monomers ($\Phi_\Delta = 0.023$) (Fig. 3b, d and S7). Parallel evaluation of photothermal effects under 808 nm laser irradiation demonstrated that J-aggregates achieved rapid temperature elevation to 47.7 °C within 3 min (0.5 W cm^{-2}, 5 min), contrasting with the negligible monomeric response ($\Delta T = 4.6$ °C) (Fig. 3c and S8). Photothermal conversion efficiency (η), calculated *via* an established method,[81] reached 47.69% for aggregates *versus* 3.59% for monomers (Fig. 3d and S9). Collectively, these data demonstrate that J-aggregation of **FUC-Se** simultaneously amplifies both photodynamic and photothermal efficacy.

DFT calculation and natural transition orbital analysis

To decipher the photophysical origins of J aggregation-enhanced ROS and heat performance, we conducted systematic DFT calculations and NTO analysis. For monomeric **FUC-Se**, both excitation and emission processes involve conventional locally excited (LE) transitions, as evidenced by the compact electron–hole distribution (centroid distance < 1 Å) in NTOs (Fig. 3e, S9 and Tables S5–S6). This localized character results in a large S_1–T_1 energy gap ($\Delta E_{ST} = 0.58$ eV) and weak spin–orbit coupling (SOC = 0.78 cm^{-1}), thus limiting intersystem crossing efficiency. Strikingly, J-aggregation induces a paradigm shift in excited-state dynamics. Initial excitation generates degenerate S_1/S_2 states through HOMO → LUMO transitions (Fig. 3f, S10 and Tables S7–S8), which rapidly split into two distinct states: (1) a low-lying S_1 state dominated by intermolecular charge-transfer excitation (CTE) with HOMO → LUMO transition across adjacent molecules (electron–hole separation, 5.5 Å), and (2) an S_2 state retaining intramolecular LE character *via* HOMO-1 → LUMO transition. Notably, the formation of this intermolecular CT state fundamentally distinguishes the photophysics of **FUC-Se** J-aggregates from those driven solely by exciton delocalization in conventional J-aggregates. While exciton delocalization typically leads to bathochromic shifts and altered radiative rates, the key feature here is the spatially separated electron–hole distribution across molecular units. This CT character directly reduces ΔE_{ST} by 43% (0.25 eV *vs.* 0.58 eV) and enhances SOC nearly tenfold (7.14 cm^{-1} *vs.* 0.78 cm^{-1}), which are not inherently provided by excitonic coupling alone (Fig. 3g). Both synergistically promote ISC, accounting for the observed sixfold increase in $^1O_2$ quantum yield, which is consistent with the El-Sayed rule:[82,83]

$$k_{ISC} \propto |\langle S|HSOC|T\rangle|^2/\Delta E^2$$

Moreover, the CT-J architecture concurrently promotes efficient non-radiative decay, establishing a stronger photothermal pathway compared to the monomer. Firstly, the CT-J aggregates exhibit a significantly larger root-mean-square deviation (RMSD = 0.209 Å) between S_0 and S_1 geometries than the monomer (RMSD = 0.118 Å). This clearly suggested pronounced structural distortion in the aggregated state upon photoexcitation (Fig. S10 and S11). This distortion would enhance vibrational energy release during $S_1 \rightarrow S_0$ relaxation, directly contributing to heat generation. Secondly, the reorganization energy of the CT-J aggregates ($\lambda_h = 0.25$ eV) is more than double that of the monomer ($\lambda_h = 0.11$ eV), demonstrating a stronger propensity for non-radiative decay over radiative transitions. Correspondingly, the k_r/k_{nr} ratio of CT-J aggregates is drastically reduced to 0.003, far lower than that of the monomer (0.111). Additionally, the CTE state's low energy position (1.38 eV *vs.* 1.70 eV in monomer) creates a thermodynamic sink for rapid internal conversion, favoring absorbed photons into lattice vibrations.[84]

Ultrafast excited-state dynamics behaviors

Following closely behind, femtosecond transient absorption spectroscopy further unraveled distinct excited-state dynamics between monomers and J-aggregates. For monomers, symmetric ground-state bleaching (GSB) ($\Delta A < 0$ at 660 nm) and excited-state absorption (ESA) ($\Delta A > 0$ at 550 nm) signals exhibited identical decay kinetics with matched lifetimes ($\tau_1 \approx 300$ ps, $\tau_2 \approx 1.5$ ns), indicative of direct $S_1 \rightarrow S_0$ relaxation without intermediate states (Fig. 4a–c). In stark contrast, J-aggregates displayed a three-component ESA decay profile dominated by an ultrafast process ($\tau_1 = 1.0$ ps, $\alpha_1 = 7.21\%$), absent in GSB dynamics (Fig. 4d–f). This unambiguously signals the formation of a charge-transfer intermediate state (CT) with near-unity yield (>95%), which is absent in the monomer and not a typical feature of excitonic J-aggregates, providing direct time-resolved evidence for a unique relaxation funnel induced by Se/π-directed assembly. This allows us to decouple the CT-mediated processes from generic aggregation effects. The CT state displays a biphasic relaxation: (i) initial vibrational cooling within 16.1 ps (τ_2), followed by (ii) non-radiative decay to the ground state over 489 ps (τ_3). The latter component's lifetime aligns with the enhanced SOC constant (7.14 cm^{-1}) and reduced S_1–T_1 gap (0.25 eV), synergistically promoting ISC-mediated $^1O_2$ generation. Concurrently, the ultrafast CT formation (1.0 ps) and vibronic coupling ($\tau_2 = 16.1$ ps) channel more absorbed energy into lattice vibrations, as evidenced by the negligible fluorescence quantum yield (Fig. 4g). Overall, the ultrafast CT formation and its subsequent relaxation (vibrational cooling and ISC-competent decay) specifically channel energy into the enhanced ROS and heat production observed, rather than through exciton delocalization pathways that would primarily affect radiative properties.

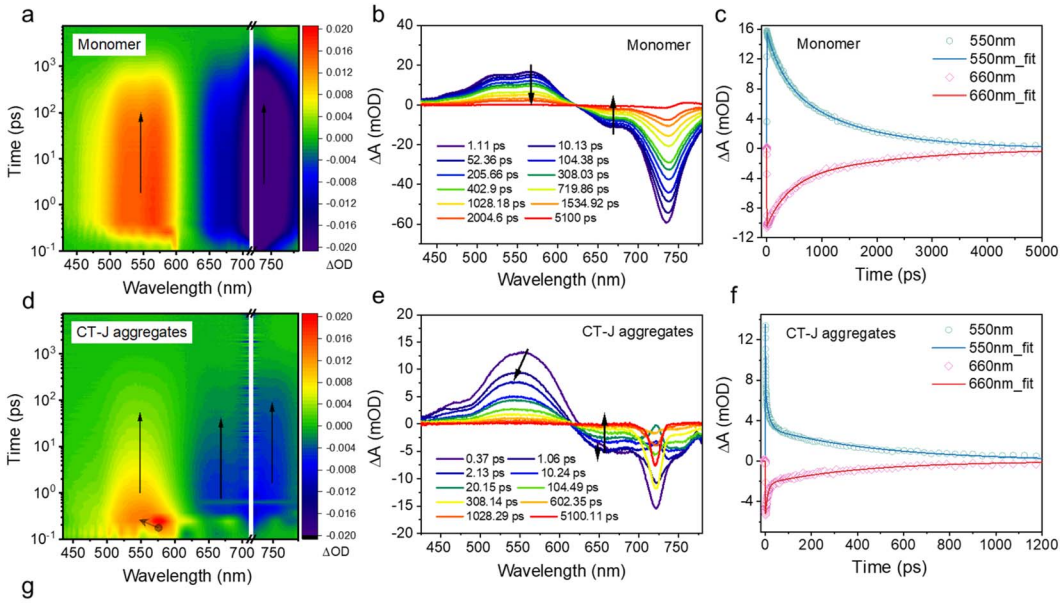

g

Monomer	τ_1	α_1	τ_2	α_2	τ_3	α_3	J-aggregate	τ_1	α_1	τ_2	α_2	τ_3	α_3
ESA (550 nm)	289 ps	5.76%	1365 ps	9.84%			ESA (550 nm)	1.0 ps	7.21%	16.1 ps	3.68%	489 ps	3.26%
GSB (660 nm)	376 ps	5.54%	1900 ps	4.88%			GSB (660 nm)	—	—	10.8 ps	3.06%	414 ps	2.23%

Fig. 4 Mechanistic study using fs-TA spectra. (a and d) Full contour maps of fs-TA spectra of **FUC-Se** monomer and J-aggregate under excitation at 725 nm (200 nJ). (b and e) fs-TA spectra of **FUC-Se** monomer and J-aggregate at selected decay times. The arrow indicates the direction of the representative wavelength along the increase of decay time. (c and f) Kinetic decay curves of ground-state bleaching (GSB) at 660 nm and excited-state absorption (ESA) at 550 nm and their fitting lines (solid line). (g) Fitting parameters of GSB and ESA of **FUC-Se** monomer and J-aggregate.

Preparation and characterization of morphology-reshaped CT-J aggregates (FUC-Se@LP)

To address the incompatibility of micron-scale **FUC-Se** J-aggregates (sheet-like structures) in biological systems, we further restructured them into spherical nanoparticles using DSPE-PEG2K *via* a thin-film dispersion method (Fig. 5a). Systematic evaluation of DSPE-PEG2K/**FUC-Se** mass ratios (1 : 4–20 : 1) revealed distinct phase behaviors (Fig. 5b, c and Tables S9–S10). In detail, low ratios (1 : 4–1 : 3) preserved J-aggregate absorption at ~800 nm but retained oversized particles (>2000 nm); intermediate ratios (1 : 2–2 : 1) reduced size to >500 nm but still unsuitable for the EPR effect; high ratios (8 : 1–20 : 1) induced obvious dissociation of J-aggregates. Optimal ratios (4 : 1–8 : 1) balanced J-aggregate integrity (~800 nm) with a hydrodynamic diameter of ~100 nm. NIR-II fluorescence analysis further showed enhanced emission at intermediate ratios (1 : 2–8 : 1), peaking at 8 : 1 due to partial monomer dissociation. Finally, the 6 : 1 formulation emerged as ideal, exhibiting ~80 nm hydrodynamic diameter (DLS), ~60 nm SEM-measured size, and strong J-aggregate fluorescence, thereby enabling cellular uptake and EPR-driven tumor targeting. And, the preservation of the distinct spectral signature suggests that the core electronic structure of the CT-J aggregate remains intact after morphological reshaping. Furthermore, the optimized **FUC-Se@LP** formulation (6 : 1 mass ratio) exhibited excellent colloidal stability, with negligible changes in hydrodynamic diameter and zeta potential over 8 days in PBS at 4 °C (Tables S9 and S10), meeting the prerequisite for *in vivo* applications. Notably, the **FUC-Se@LP** nanoparticles demonstrated stability in a physiologically relevant environment. The characteristic J-aggregate absorption at ~800 nm remained intact after incubation in PBS and RMMI 1640 containing 10% fetal bovine serum at 37 °C for up to 24 hours (Fig. S12), confirming the robustness of the CT-J core against dissociation in media simulating *in vivo* conditions. In addition to spectral characterization, molecular dynamics simulations further visualized the DSPE-PEG-assisted aggregation and assembly process of **FUC-Se**, which still retained the characteristics of J-aggregation in nanoparticles (Video S2 and Fig. S13). The simulations explicitly show that the directional π–π stacking and Se···Se interactions, key to forming the CT state, are maintained within the nanoparticle core during the encapsulation process. This optimized **FUC-Se@LP** nanoparticle system was selected for subsequent biological studies.

In vitro ROS generation and photothermal performance of FUC-Se@LP

Before evaluating the anticancer potential of **FUC-Se@LP**, we first examined whether morphological reshaping affected its ROS generation and photothermal properties. SOSG and DHR123 were used to detect $^1O_2$ and superoxide anions ($O_2^{-\bullet}$), respectively. As shown in Fig. 5d and S14, **FUC-Se** (sheet J-aggregates) and **FUC-Se@LP** (spherical nanoparticles) showed comparable enhancement in either SOSG or DHR123 under identical

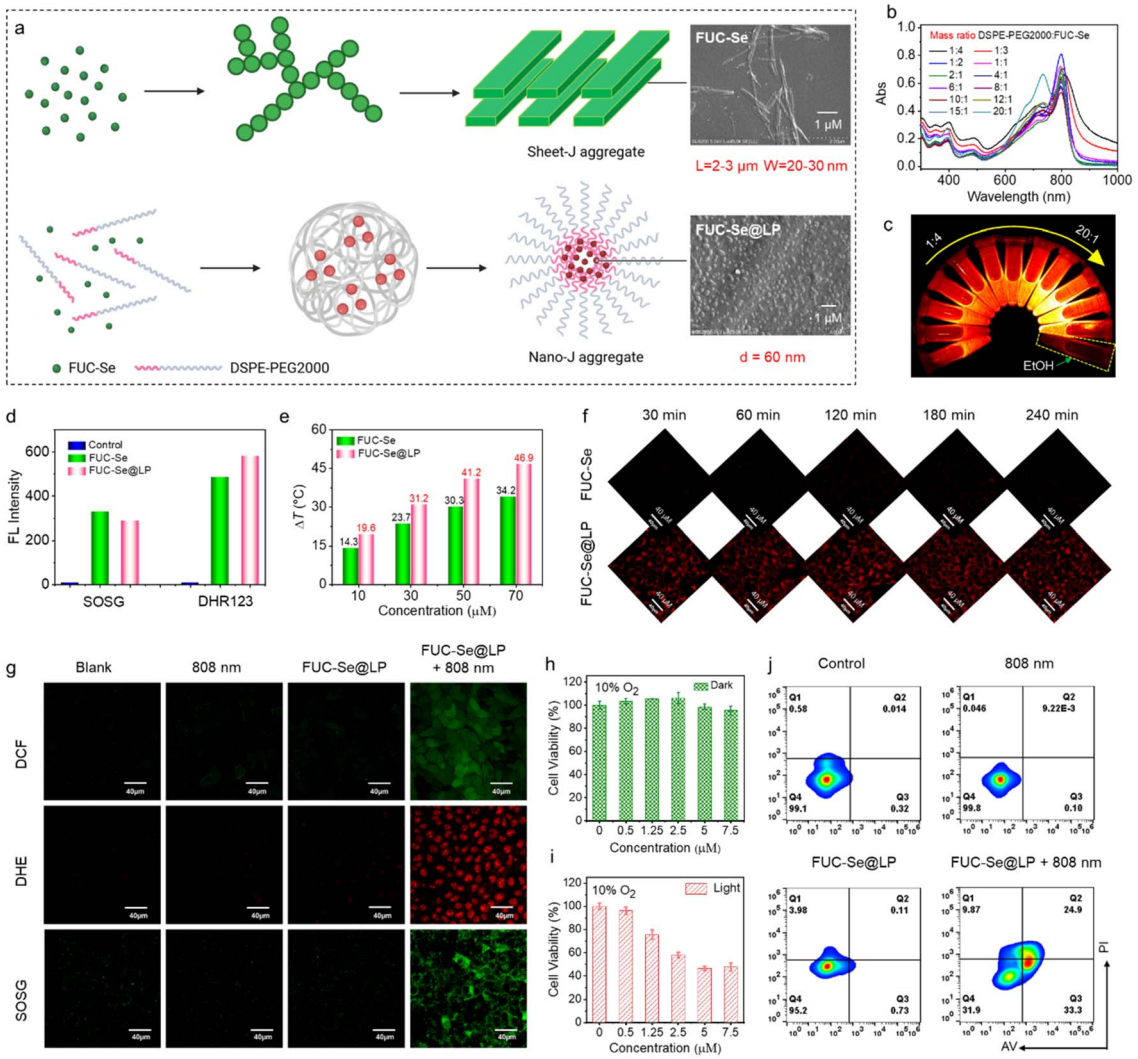

Fig. 5 Morphology remodeling process and performance verification at *in vitro* and cellular levels. (a) Schematic diagram of the preparation process of **FUC-Se** morphology remodeling; scale bar: 1 μm. (b) Absorption spectra of **FUC-Se** nanoparticles prepared with different mass ratios. (c) NIR-II fluorescence images of **FUC-Se** nanoparticles prepared with different mass ratios. Comparison of *in vitro* performance of **FUC-Se** and **FUC-Se@LP**. (d) *In vitro* singlet oxygen and superoxide anion detection indicated by SOSG and DHR123 as fluorescence probes, respectively (808 nm, 100 mW cm^{-2}, 6 min). (e) Concentration-dependent photothermal heating performance under identical absorbance and irradiation conditions (808 nm, 800 mW cm^{-2}, 5 min). (f) Confocal fluorescence imaging cell uptake of **FUC-Se** and **FUC-Se@LP**; scale bar: 40 μm. (g) Confocal fluorescence imaging of intracellular reactive oxygen species production induced by **FUC-Se@LP** (808 nm, 100 mW cm^{-2}, 5 min); scale bar: 40 μm. (h) Dark cytotoxicity and (i) photocytotoxicity of **FUC-Se@LP** in mild hypoxia (10% O_2 + 5% CO_2) (808 nm, 100 mW cm^{-2}, 5 min). (j) Apoptosis analysis of 4T1 cells under different treatments by flow cytometry using AV-FITC and PI as indicators.

conditions, suggesting that morphological remodeling has negligible impact on ROS generation. ESR spin-trapping experiments using DMPO (for $O_2^{-\bullet}$) and TEMP (for $^1O_2$) confirmed the concurrent generation of both radical and non-radical ROS species upon irradiation (Fig. S15). Next, we further assessed their photothermal performance. As shown in Fig. 5e and S16, **FUC-Se@LP** exhibited significantly higher temperature elevations than **FUC-Se** across various concentrations and laser power densities. The photothermal conversion efficiency of **FUC-Se@LP** reached 52.6%, outperforming the 16% efficiency of ICG. Subsequently, photostability was further evaluated using ICG as a reference (Fig. S17). Within five minutes, ICG's absorption dropped below 0.1, indicating near complete degradation. **FUC-Se** retained absorbance above 0.3 at five minutes but declined to near zero after ten minutes. In contrast, **FUC-Se@LP** maintained absorbance above 0.45 throughout. Overall, compared to sheet J-aggregates (**FUC-Se**), **FUC-Se@LP** not only preserves comparable ROS generation capacity but also exhibits superior photostability and enhanced photothermal performance.

Enhanced cellular uptake and mitochondrial targeting

Critically, the reshaped J-aggregates **FUC-Se@LP** exhibited significantly accelerated cellular internalization kinetics. Real-time confocal imaging revealed rapid intracellular accumulation of **FUC-Se@LP**, with intense red fluorescence saturation achieved within 30 minutes of treatment (Fig. 5f). This uptake

kinetics starkly contrasted with negligible fluorescence in cells treated with non-engineered **FUC-Se** aggregates. Fluorescence imaging further demonstrated exceptional subcellular targeting precision. As shown in Fig. S18, **FUC-Se@LP** showed strong colocalization with MitoTracker TMRM (Pearson's coefficient = 0.85), confirming mitochondria-specific localization. This dual advantage of accelerated cellular uptake and organelle-level spatial precision creates favorable conditions for phototherapy, as mitochondrial targeting maximizes ROS-induced oxidative damage while minimizing off-target effects.[85,86]

Dual-mode ROS generation and phototoxicity

Previous *in vitro* studies further established **FUC-Se@LP** as a dual-mode photosensitizer capable of simultaneously generating singlet oxygen and superoxide anions under 808 nm irradiation. To validate its cellular performance, we employed three fluorescent probes, including DCFH-DA for pan-ROS detection,[7,80,87] SOSG for $^1O_2$-specific tracking, and DHE for $O_2^{-\bullet}$ monitoring. As shown in Fig. 5g, neither **FUC-Se@LP** alone nor laser irradiation independently induced significant intracellular ROS production. However, laser-activated **FUC-Se@LP** triggered a synergistic ROS cascade, evidenced by concurrent fluorescence intensification across all probes, confirming efficient dual ROS generation. Crucially, this cooperative mechanism maintains ROS production efficiency under mild hypoxia, relieving the oxygen-dependent limitation of conventional photodynamic therapy. The cytotoxic effects correlated directly with ROS generation profiles. **FUC-Se@LP** exhibited exceptional biocompatibility under dark conditions, preserving >90% 4T1 cell viability even at 7.5 μM (Fig. 5h). Upon laser activation, it demonstrated concentration-dependent phototoxicity (10% O_2, IC_{50} = 2.47 μM) (Fig. 5i). Importantly, this potent efficacy was retained even under severe hypoxia (2% O_2), with a comparable IC_{50} value (Fig. S19). This robust hypoxia tolerance underscores the advantage of the CT-J aggregate-enabled dual-mode ROS mechanism, where the oxygen-independent Type-I pathway remains highly operative under oxygen-deficient conditions.

To elucidate the mechanism of **FUC-Se@LP**-induced cell death, AV-FITC/PI staining was performed (Fig. 5j). Neither **FUC-Se@LP** alone nor 808 nm laser irradiation independently triggered apoptosis or necrosis (apoptotic rate < 5%). However, their combined application markedly elevated apoptotic cells to 58.2%. This apoptosis-dominant response aligns with the mitochondrial

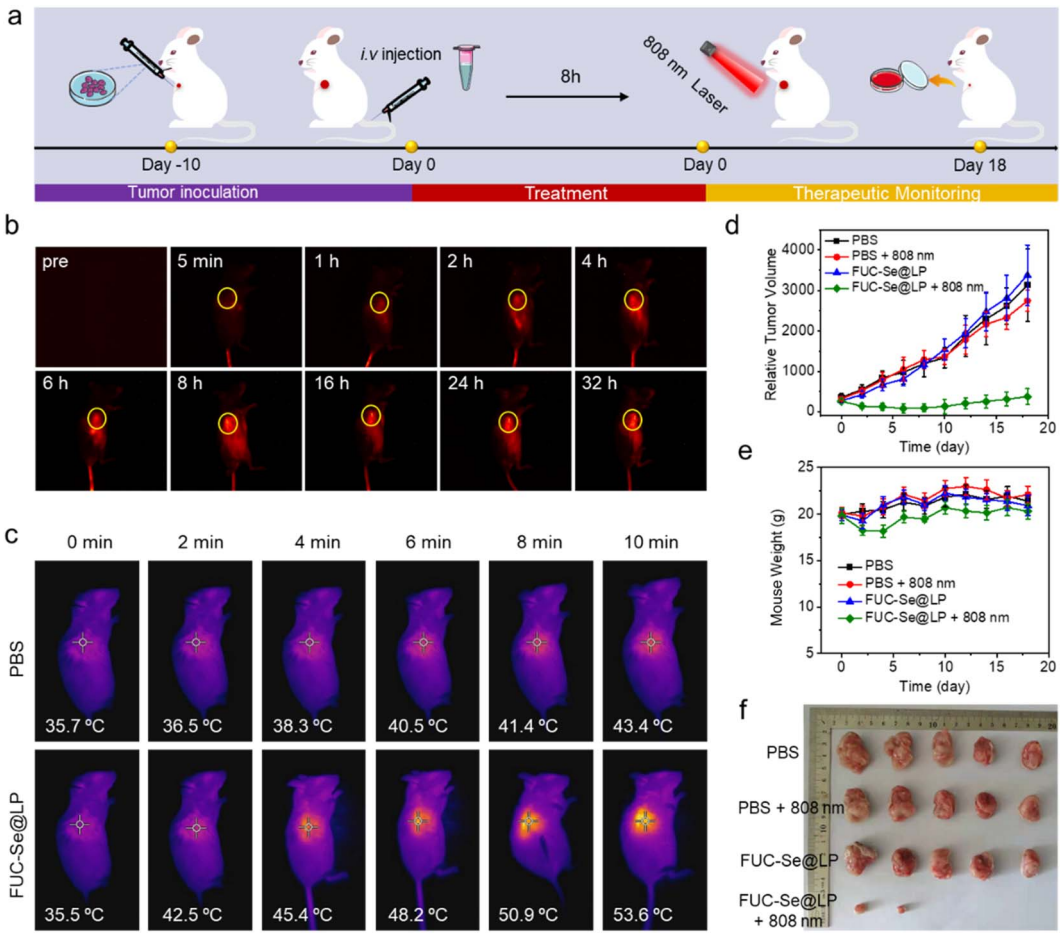

Fig. 6 *In vivo* distribution and anti-subcutaneous tumor treatment of **FUC-Se@LP**. (a) Schematic illustration of the treatment schedule of **FUC-Se@LP**. (b) *In vivo* NIR-II fluorescence images of 4T1-tumor-bearing mice at different time points after intravenous injection of **FUC-Se@LP** in PBS. (c) Thermal IR images of 4T1-tumor-bearing mice after intravenous injection of **FUC-Se@LP** or PBS under same irradiation (808 nm, 0.8 W cm^{-2}, 10 min). (d) Tumor volume, (e) body weight changes, and (f) representative tumor images of mice from different treatment groups.

targeting specificity observed in prior mitochondrial colocalization experiments, indicating that localized ROS generation at mitochondrial sites preferentially activates intrinsic apoptotic pathways.[80] These findings collectively position **FUC-Se@LP** as a hypoxia-tolerant phototherapeutic agent that synergizes dual ROS generation, mitochondrial precision targeting, and apoptosis-dominated cytotoxicity for solid tumor treatment.

In vivo distribution and anti-subcutaneous tumor treatment of FUC-Se@LP

Prior to evaluating therapeutic efficacy, we first characterized the tumor-targeting capability of **FUC-Se@LP** through real-time NIR-II fluorescence imaging. As shown in Fig. 6a and b, following intravenous administration, time-lapsed imaging revealed progressive tumor accumulation commencing at 2 h

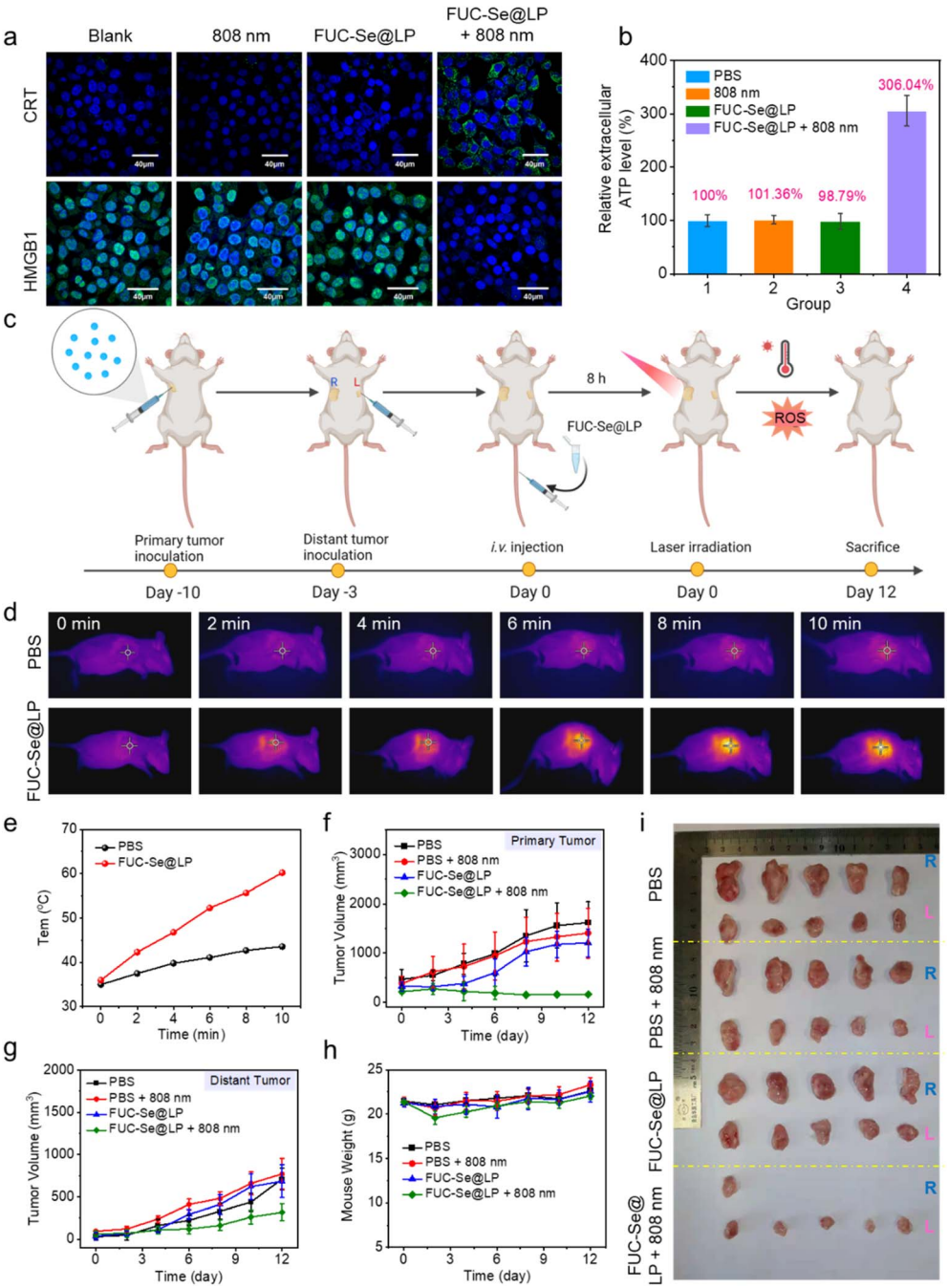

Fig. 7 Validation of the antitumor effect of **FUC-Se@LP** against primary and distant tumors. (a) Immunofluorescent imaging of CRT and HMGB1; scale bar: 40 μm, (b) The relative extracellular ATP level in 4T1 cells after different treatments. (c) Schematic illustration the treatment schedule of **FUC-Se@LP**. (d) Thermal IR images and (e) the corresponding temperature change curves of 4T1-tumor-bearing mice after intravenous injection of **FUC-Se@LP** or PBS under same irradiation (808 nm, 0.8 W cm^{-2}, 10 min). (f) The primary and (g) distant tumor volume changes of mice from each group during treatments. (h) Body weight changes of mice during different treatments. (i) The photograph of tumors from each group at day 12 after treatments.

post-injection, peaking at 8 h, and maintaining sustained retention through 24 h. This spatiotemporal profiling established the optimal therapeutic window at 8 h post-injection when maximum tumor accumulation was achieved. Capitalizing on that, we conducted phototherapy in 4T1 tumor-bearing mice under 808 nm irradiation (0.8 W cm^{-2}). As shown in Fig. 6c, while PBS-injected controls exhibited a slight temperature increase, **FUC-Se@LP**-mediated photoconversion induced rapid tumor hyperthermia, reaching 46.6 °C within 4 min and 55.5 °C at 10 min, surpassing the critical threshold for protein denaturation. This localized thermal ablation translated to significant tumor regression. Phototherapy-treated tumors demonstrated significant volume reduction by Day 2 post-treatment, with complete eradication observed in 60% of subjects (3/5 mice) and only minimal residual tumors in the remaining cases (Fig. 6d and f). In stark contrast, control groups exhibited uninterrupted tumor progression. Crucially, all treatment groups maintained stable body weights throughout the observation period (Fig. 6e), confirming systemic biocompatibility.

Immunogenic cell death and anti-distant tumor effects triggered by FUC-Se@LP

Beyond direct tumor ablation, **FUC-Se@LP**-mediated phototherapy demonstrates profound immunomodulatory effects through light-triggered immunogenic cell death (ICD).[87–91] As a hallmark of ICD, the cascade release of damage-associated molecular patterns (DAMPs), including calreticulin (CRT) exposure, ATP secretion, and HMGB1 translocation, was systematically validated (Fig. 7). Confocal microscopy revealed intense CRT surface translocation exclusively in the **FUC-Se@LP** + laser group, compared to negligible signals in controls. This "eat me" signal primes antigen-presenting cells (APCs) for phagocytic activation, bridging innate and adaptive immunity. Concomitantly, HMGB1 (a nuclear DNA chaperone) underwent complete cytoplasmic relocalization and extracellular release in the treatment group, evidenced by the disappearance of nuclear green fluorescence (Fig. 7a). This spatial redistribution converts HMGB1 into a pro-inflammatory cytokine that activates Toll-like receptor 4 (TLR4) on dendritic cells, driving their maturation. The ICD cascade culminated 3-fold increase in ATP efflux (Fig. 7b), establishing a chemoattractant gradient for immune cell recruitment. These results indicate that **FUC-Se@LP** can effectively enhance the immunogenicity of 4T1 cells. Crucially, this immunogenic potential is strictly light-gated: **FUC-Se@LP** alone showed no DAMP release, ensuring spatiotemporal control over immune activation.

The therapeutic implications of this ICD induction were validated in a bilateral 4T1 tumor model, where primary (right flank) and distant (left axilla) tumors were sequentially inoculated (Fig. 7c). Notably, temperature monitoring confirmed precise photothermal control: primary tumors reached ~60 °C (sufficient for cell death) *versus* ~40 °C in laser-only controls (Fig. 7d and e). Localized treatment of primary tumors (0.8 W cm^{-2} for 10 min) achieved complete ablation in 80% of subjects (4/5 mice) while suppressing distant tumor growth by 58% *versus* PBS controls (Fig. 7f–g and i). Systemic safety was concurrently demonstrated through stable body weight trajectories (Fig. 7h) and histologically confirmed organ integrity, with no hepatic inflammation, renal fibrosis, or pulmonary lesions observed (Fig. S20), demonstrating that the remodeled J-aggregate **FUC-Se@LP** exhibits excellent biocompatibility. These multimodal therapeutic advantages, combined with NIR-II imaging-guided treatment personalization, position **FUC-Se@LP** as a transformative candidate for clinical translation, particularly for treating hypoxic, immunotherapy-resistant malignancies.

Conclusions

In this study, we successfully developed a charge-transfer state J-aggregate photosensitizer (**FUC-Se**). By leveraging a unique CT-J aggregation mechanism, these aggregates exhibit a bathochromic shift of 80 nm (λ_{abs} = 810 nm) and reconfigured energy landscapes. This restructuring reduces the singlet–triplet gap to 0.25 eV (*vs.* 0.58 eV in monomers) and amplifies spin–orbit coupling to 7.14 cm^{-1} (9.2-fold enhancement). Concurrently, it also promotes a 77% surge in geometry reorganization ($RMSD_{S1\rightarrow S0}$ = 0.209 *vs.* 0.118) and a 127% increase in the Huang–Rhys factor (λ_h = 0.25 eV *vs.* 0.11 eV). Consequently, the ISC efficiency and vibronic heat conversion are significantly boosted, with a Φ_Δ of 0.139 (a 6-fold increase over the monomer) and an η of 47.69% (a 13-fold improvement). Notably, **FUC-Se** achieves spontaneous aggregation at ultralow concentrations without requiring exogenous triggers. Subsequent phospholipid remodeling yields tumor-targeted nanospheres (**FUC-Se@LP**) capable of hypoxia-insensitive PDT/PTT and NIR-II fluorescence-guided imaging. *In vivo*, **FUC-Se@LP** eradicates primary tumors *via* ROS/thermal synergy (IC_{50} = 2.47 μM) and suppresses distant lesions by 58% through the induction of immunogenic death, all while demonstrating excellent biosafety. This work establishes CT-J aggregation as a new design strategy, offering potential for improved clinical metastasis management.

Ethical statement

All the animal experiments were performed in accordance with the Guide for the Care and Use of Laboratory Animals published by the National Institutes of Health. The animal protocol was approved by the local research ethics review board of the Animal Ethics Committee of Dalian University of Technology (Certificate number//Ethics approval no. is 2018-043).

Author contributions

D. M., H. B., X. C., and X. P. conceived and designed the experiments for this project. D. M. and H. B. performed the synthetic work, carried out the characterization of the compounds, and conducted spectroscopic measurements, other *in vitro* assays, cellular assays, and mouse experiments. F. P. was responsible for the molecular dynamics simulations, while D. Z. and P. Z. conducted the theoretical calculations. Z.

C. and X. H. performed the crystal structure analysis. H. G., Y. G., and Y. W. assisted in the measurement and analysis of selected spectroscopic data. L. W. contributed to the data analysis and manuscript revision. X. C. and X. P. supervised the work.

Conflicts of interest

The authors declare no competing financial interests.

Data availability

CCDC 2431831 contains the supplementary crystallographic data for this paper.[92]

The data supporting this article have been included as part of the supplementary information (SI). Supplementary information is available. See DOI: https://doi.org/10.1039/d5sc08871b.

Acknowledgements

This work was supported by the Major Program of the National Natural Science Foundation of China (Grant No. 22090010 and 22090011), the GuangDong Basic and Applied Basic Research Foundation (Grant No. 2023B1515120001), and the Shenzhen University 2035 Program for Excellent Research (Grant No. 00000208 and 00000225). D. M. acknowledges the support from the China Postdoctoral Science Foundation (Grant No. 2024M752118) and the Young Scientists Fund of the National Natural Science Foundation of China (Grant No. 22408232).

Notes and references

1 D. Ma, H. Bian, M. Gu, L. Wang, X. Chen and X. Peng, Recent advances in the design and applications of near-infrared II responsive small molecule phototherapeutic agents, *Coord. Chem. Rev.*, 2024, **505**, 215677.
2 X. Zhao, J. Du, W. Sun, J. Fan and X. Peng, Regulating Charge Transfer in Cyanine Dyes: A Universal Methodology for Enhancing Cancer Phototherapeutic Efficacy, *Acc. Chem. Res.*, 2024, **57**(17), 2582–2593.
3 X. Zhao, J. Liu, J. Fan, H. Chao and X. Peng, Recent progress in photosensitizers for overcoming the challenges of photodynamic therapy: from molecular design to application, *Chem. Soc. Rev.*, 2021, **50**(6), 4185–4219.
4 H. Bian, D. Ma, F. Pan, X. Zhang, K. Xin, X. Zhang, Y. Yang, X. Peng and Y. Xiao, Cardiolipin-Targeted NIR-II Fluorophore Causes "Avalanche Effects" for Re-Engaging Cancer Apoptosis and Inhibiting Metastasis, *J. Am. Chem. Soc.*, 2022, **144**(49), 22562–22573.
5 X. Kang, Z. Du, S. Yang, M. Liang, Q. Liu and J. Qi, Smart molecular probes with controllable photophysical property for smart medicine, *Smart Mol.*, 2024, **2**(3), e20240033.
6 H. Kim, Y. Lee, H. Jeong, J. Lee, X. Wu, H. Li and J. Yoon, Photodynamic and photothermal therapies for bacterial infection treatment, *Smart Mol.*, 2023, **1**(1), e20220010.
7 H. Gu, W. Sun, J. Du, J. Fan and X. Peng, Dual-acceptor engineering of donor-acceptor type molecules for all-round boosting anti-tumor phototherapy, *Smart Mol.*, 2023, **2**(2), e20230014.
8 Y. Dai, J. Sun, X. Zhang, J. Zhao, W. Yang, J. Zhou, Z. Gao, Q. Wang, F. Yu and B. Wang, Supramolecular assembly boosting the phototherapy performances of BODIPYs, *Coord. Chem. Rev.*, 2024, **517**, 216054.
9 N. Dar and R. Ankari, Theoretical Models, Preparation, Characterization and Applications of Cyanine J-Aggregates: A Minireview, *ChemistryOpen*, 2022, **11**(11), e20220010.
10 X. Hu, C. Zhu, F. Sun, Z. Chen, J. Zou, X. Chen and Z. Yang, J-Aggregation Strategy toward Potentiated NIR-II Fluorescence Bioimaging of Molecular Fluorophores, *Adv. Mater.*, 2023, **36**(1), 2304848.
11 J. H. Kim, T. Schembri, D. Bialas, M. Stolte and F. Würthner, Slip-Stacked J-Aggregate Materials for Organic Solar Cells and Photodetectors, *Adv. Mater.*, 2021, **34**(22), 2104678.
12 P. Kumari, S. Arora, Y. Pan, I. Ahmed, S. Kumar and B. Parshad, Tailoring Indocyanine Green J-Aggregates for Imaging, Cancer Phototherapy, and Drug Delivery: A Review, *ACS Appl. Bio Mater.*, 2024, **7**(8), 5121–5135.
13 G. Sun, Y. Zhang, N. Zhou, F. Huo and C. Yin, Recent advances in the construction, imaging and phototherapy applications of NIR-II J-aggregates based on different fluorophores, *Dyes Pigm.*, 2025, **243**, 113054.
14 Y. Tian, D. Yin and L. Yan, J-aggregation strategy of organic dyes for near-infrared bioimaging and fluorescent image-guided phototherapy, *Wiley Nanomed. Nanobiotechnology*, 2022, **15**(1), e1831.
15 J. Xu, X. Zheng, T. Ren, L. Shi, X. Yin, L. Yuan and X. Zhang, Recent advances in near-infrared-II organic J-aggregates for bio-applications, *Coord. Chem. Rev.*, 2025, **528**, 216379.
16 S. Xu, H. Liu, S. Huan, L. Yuan and X. Zhang, Recent progress in utilizing near-infrared J-aggregates for imaging and cancer therapy, *Mater. Chem. Front.*, 2021, **5**(3), 1076–1089.
17 K. Li, X. Duan, Z. Jiang, D. Ding, Y. Chen, G. Zhang and Z. Liu, J-aggregates of meso-[2.2]paracyclophanyl-BODIPY dye for NIR-II imaging, *Nat. Commun.*, 2021, **12**(1), 2376.
18 C. Sun, B. Li, M. Zhao, S. Wang, Z. Lei, L. Lu, H. Zhang, L. Feng, C. Dou, D. Yin, H. Xu, Y. Cheng and F. Zhang, J-Aggregates of Cyanine Dye for NIR-II *in Vivo* Dynamic Vascular Imaging beyond 1500 nm, *J. Am. Chem. Soc.*, 2019, **141**(49), 19221–19225.
19 C. Sun, X. Sun, P. Pei, H. He, J. Ming, X. Liu, M. Liu, Y. Zhang, Y. Xia, D. Zhao, X. Li, Y. Xie and F. Zhang, NIR-II J-Aggregates Labelled Mesoporous Implant for Imaging-Guided Osteosynthesis with Minimal Invasion, *Adv. Funct. Mater.*, 2021, **31**(23), 2100656.
20 S. Usama, D. Caldwell, P. Shrestha, M. Luciano, N. Patel, J. Kalen, J. Ivanic and M. Schnermann, Modified norcyanines enable ratiometric pH imaging beyond 1000 nm, *Biosens. Bioelectron.*, 2022, **217**, 114610.
21 C. Zhang, Y. Wu, F. Zeng, Y. Wen, J. Chen, G. Deng, L. Zhang, S. Zhao, S. Wu and Y. Zhao, Structurally Modulated Formation of Cyanine J-Aggregates with Sharp and

Tunable Spectra for Multiplexed Optoacoustic and Fluorescence Bioimaging, *Angew. Chem., Int. Ed.*, 2024, **63**(34), e202406694.

22 Q. Zhang, P. Yu, Y. Fan, C. Sun, H. He, X. Liu, L. Lu, M. Zhao, H. Zhang and F. Zhang, Bright and Stable NIR-II J-Aggregated AIE Dibodipy-Based Fluorescent Probe for Dynamic *in Vivo* Bioimaging, *Angew. Chem., Int. Ed.*, 2020, **60**(8), 3967–3973.

23 Y. Zhu, P. Wu, S. Liu, J. Yang, F. Wu, W. Cao, Y. Yang, B. Zheng and H. Xiong, Electron-Withdrawing Substituents Allow Boosted NIR-II Fluorescence in J-Type Aggregates for Bioimaging and Information Encryption, *Angew. Chem., Int. Ed.*, 2023, **62**(47), e202313166.

24 X. Bao, S. Zheng, L. Zhang, A. Shen, G. Zhang, S. Liu and J. Hu, Nitric-Oxide-Releasing aza-BODIPY: A New Near-Infrared J-Aggregate with Multiple Antibacterial Modalities, *Angew. Chem., Int. Ed.*, 2022, **61**(32), e202207250.

25 D. Chen, Y. Xu, Y. Wang, C. Teng, X. Li, D. Yin and L. Yan, J-aggregates of strong electron-donating groups linked Aza-BODIPY adjusting by polypeptide for NIR-II phototheranostics, *Spectrochim. Acta, Part A*, 2024, **322**, 124789.

26 C. Ou, Z. Zhao, L. An, L. Zheng, F. Gao, Q. Zhu, W. Wang, J. Shao, L. Xie and X. Dong, J-Aggregate Promoting NIR-II Emission for Fluorescence/Photoacoustic Imaging-Guided Phototherapy, *Adv. Healthcare Mater.*, 2024, **13**(23), 2400846.

27 F. Tang, H. Yu, Y. Huang, X. Zhao, Z. Chen, H. Ma, B. Zheng, M. Ke, Y. Zhang, X. Li, J. Yoon and J. Huang, Phthalocyanine J-aggregate nanoparticles with enormous-redshifted and intense absorption: Potential structure-J-aggregation relationships and application in tumor-associated macrophages-targeted phototheranostics, *Chem. Eng. J.*, 2024, **496**, 154272.

28 Y. Wan, Y. Gao, W. Wei, K. Lee, J. Tan, C. Chen, H. Chen, S. Li, K. Wong and C. Lee, Facilely Achieving Near-Infrared-II J-Aggregates through Molecular Bending on a Donor-Acceptor Fluorophore for High-Performance Tumor Phototheranostics, *ACS Nano*, 2024, **18**(41), 27949–27961.

29 Y. Xu, X. Meng, Y. Zhao, M. Jia, H. Zhu, J. Song, Y. Su, W. Qiao, J. Qi and Z. Y. Wang, Pyrrolopyrrole Cyanine J-Aggregate Nanoparticles with High Near-Infrared Fluorescence Brightness and Photothermal Performance for Efficient Phototheranostics, *ACS Appl. Mater. Interfaces*, 2024, **16**(30), 39005–39020.

30 Y. Kang, W. Chen, K. Teng, L. Wang, X. Xu, L. Niu, G. Cui and Q. Yang, Aggregation Turns BODIPY Fluorophores into Photosensitizers: Reversibly Switching Intersystem Crossing On and Off for Smart Photodynamic Therapy, *CCS Chem.*, 2022, **4**(11), 3516–3528.

31 Y. Li, T. Ma, H. Jiang, W. Li, D. Tian, J. Zhu and Z. Li, Anionic Cyanine J-Type Aggregate Nanoparticles with Enhanced Photosensitization for Mitochondria-Targeting Tumor Phototherapy, *Angew. Chem., Int. Ed.*, 2022, **61**(24), e202203093.

32 Y. Liu, G. Liu, W. Zhou, G. Feng, Q. Ma, Y. Zhang and G. Xing, In Situ Self-Assembled J-Aggregate Nanofibers of Glycosylated Aza-BODIPY for Synergetic Cell Membrane Disruption and Type I Photodynamic Therapy, *Angew. Chem., Int. Ed.*, 2023, **62**(40), e202309786.

33 J. Xue, Q. Liang, R. Wang, J. Hou, W. Li, Q. Peng, Z. Shuai and J. Qiao, Highly Efficient Thermally Activated Delayed Fluorescence via J-Aggregates with Strong Intermolecular Charge Transfer, *Adv. Mater.*, 2019, **31**(28), 1808242.

34 S. Li, X. Yan, J. Zhang, X. Guo, Y. Zhang, M. Su, C. Yang, H. Zhang and C. Li, J-Aggregation-Driven Supramolecular Assembly of Dye-Conjugated Block Polymers: From Morphological Tailoring to Anticancer Applications, *Adv. Funct. Mater.*, 2021, **31**(51), 2105189.

35 M. Su, Q. Han, X. Yan, Y. Liu, P. Luo, W. Zhai, Q. Zhang, L. Li and C. Li, A Supramolecular Strategy to Engineering a Non-photobleaching and Near-Infrared Absorbing Nano-J-Aggregate for Efficient Photothermal Therapy, *ACS Nano*, 2021, **15**(3), 5032–5042.

36 Y. Tian, D. Yin, Q. Cheng, H. Dang, C. Teng and L. Yan, Supramolecular J-aggregates of aza-BODIPY by steric and π–π nteractions for NIR-II phototheranostics, *J. Mater. Chem. B*, 2022, **10**(10), 1650–1662.

37 X. Guo, W. Sheng, H. Pan, L. Guo, H. Zuo, Z. Wu, S. Ling, X. Jiang, Z. Chen, L. Jiao and E. Hao, Tuning Shortwave-Infrared J-aggregates of Aromatic Ring-Fused Aza-BODIPYs by Peripheral Substituents for Combined Photothermal and Photodynamic Therapies at Ultralow Laser Power, *Angew. Chem., Int. Ed.*, 2024, **63**(11), e202319875.

38 A. Sarbu, L. Biniek, J. Guenet, P. Mésini and M. Brinkmann, Reversible J- to H-aggregate transformation in thin films of a perylenebisimide organogelator, *J. Mater. Chem. C*, 2015, **3**(6), 1235–1242.

39 C. Shen and F. Würthner, NIR-emitting squaraine J-aggregate nanosheets, *Chem. Commun.*, 2020, **56**(68), 9878–9881.

40 L. Dong, X. Shi, H. Li, Z. Liu, K. Teng, L. Niu, Z. Hu and Q. Yang, Light-Facilitated Reassembly to Generate J-Aggregates of Glucosyl aza-BODIPY with Second Near-Infrared Emission for Bioimaging, *ACS Mater. Lett.*, 2024, **6**(8), 3523–3532.

41 V. Grande, B. Soberats, S. Herbst, V. Stepanenko and F. Würthner, Hydrogen-bonded perylene bisimide J-aggregate aqua material, *Chem. Sci.*, 2018, **9**(34), 6904–6911.

42 C. Sun, M. Zhao, X. Zhu, P. Pei and F. Zhang, One-Pot Preparation of Highly Dispersed Second Near-Infrared J-Aggregate Nanoparticles Based on FD-1080 Cyanine Dye for Bioimaging and Biosensing, *CCS Chem.*, 2022, **4**(2), 476–486.

43 W. Wagner, M. Wehner, V. Stepanenko, S. Ogi and F. Würthner, Living Supramolecular Polymerization of a Perylene Bisimide Dye into Fluorescent J-Aggregates, *Angew. Chem., Int. Ed.*, 2017, **56**(50), 16008–16012.

44 Z. He, Y. Gao, Z. Huang, M. Zhan, S. Tian, F. Fang, D. Zhao, Z. Li, F. Meng, B. Tang and L. Luo, Tuning the Near-Infrared J-Aggregate of a Multicationic Photosensitizer through Molecular Coassembly for Symbiotic Photothermal Therapy and Chemotherapy, *ACS Nano*, 2025, **19**(10), 10220–10231.

45 X. Ma, Y. Huang, W. Chen, J. Liu, S. Liu, J. Yin and G. F. Yang, J-Aggregates Formed by NaCl Treatment of Aza-Coating Heptamethine Cyanines and Their Application to Monitoring Salt Stress of Plants and Promoting Photothermal Therapy of Tumors, *Angew. Chem., Int. Ed.*, 2022, **62**(3), e202216109.

46 M. Wehner and F. Würthner, Supramolecular polymerization through kinetic pathway control and living chain growth, *Nat. Rev. Chem.*, 2019, **4**(1), 38–53.

47 H. Alotaibi, T. Hatahet and W. Al-Jamal, Indocyanine green J-aggregate (IJA) theranostics: Challenges and opportunities, *Int. J. Pharm.*, 2024, **661**, 124456.

48 W. Chen, C. Cheng, E. Cosco, S. Ramakrishnan, J. Lingg, O. Bruns and J. Sletten, Shortwave Infrared Imaging with J-Aggregates Stabilized in Hollow Mesoporous Silica Nanoparticles, *J. Am. Chem. Soc.*, 2019, **141**(32), 12475–12480.

49 B. Du, R. Liu, C. Qu, K. Qian, Y. Suo, F. Wu, H. Chen, X. Li, Y. Li, H. Liu and Z. Cheng, J-aggregates albumin-based NIR-II fluorescent dye nanoparticles for cancer phototheranostics, *Mater. Today Bio*, 2022, **16**, 100366.

50 X. Guo, M. Li, H. Wu, W. Sheng, Y. Feng, C. Yu, L. Jiao and E. Hao, Near-IR absorbing J-aggregates of a phenanthrene-fused BODIPY as a highly efficient photothermal nanoagent, *Chem. Commun.*, 2020, **56**(93), 14709–14712.

51 X. Guo, J. Yang, M. Li, F. Zhang, W. Bu, H. Li, Q. Wu, D. Yin, L. Jiao and E. Hao, Unique Double Intramolecular and Intermolecular Exciton Coupling in Ethene-Bridged aza-BODIPY Dimers for High-Efficiency Near-Infrared Photothermal Conversion and Therapy, *Angew. Chem., Int. Ed.*, 2022, **61**(44), e202211081.

52 J. Liu, X. Zhang, M. Fu, X. Wang, Y. Gao, X. Xu, T. Xiao, Q. Wang and Q. Fan, A diketopyrrolopyrrole-based small molecule with an extended conjugated skeleton and J-aggregation behavior for 808 nm laser triggered phototheranostics, *Biomater. Sci.*, 2023, **11**(21), 7124–7131.

53 C. Teng, H. Dang, S. Zhang, Y. Xu, D. Yin and L. Yan, J-aggregates of Br- and piperazine-modified cyanine dye with the assistance of amphiphilic polypeptides for efficient NIR-IIa phototheranostics under 1064 nm irradiation, *Acta Biomater.*, 2022, **154**, 572–582.

54 N. Yang, S. Song, M. Akhtar, C. Liu, L. Yao, J. Yu, Y. Li, Q. Li, D. He and C. Yu, J-Aggregation induced NIR-II fluorescence: an aza-BODIPY luminogen for efficient phototheranostics, *J. Mater. Chem. B*, 2023, **11**(40), 9712–9720.

55 F. Zhao, X. Zhang, F. Bai, S. Lei, G. He, P. Huang and J. Lin, Maximum Emission Peak Over 1500 nm of Organic Assembly for Blood–Brain Barrier-Crossing NIR-IIb Phototheranostics of Orthotopic Glioblastoma, *Adv. Mater.*, 2023, **35**(22), 2208097.

56 Y. Zhao, L. Li, Q. Ye, Y. Gong, R. Yang and H. Liu, Reaction-Activated Disassembly of the NIR-II Probe Enables Fast Detection and Ratiometric Photoacoustic Imaging of Glutathione *in Vivo*, *Anal. Chem.*, 2023, **95**(37), 14043–14051.

57 Y. Zhu, F. Wu, B. Zheng, Y. Yang, J. Yang and H. Xiong, Electron-Withdrawing Substituents Enhance the Type I PDT and NIR-II Fluorescence of BODIPY J Aggregates for Bioimaging and Cancer Therapy, *Nano Lett.*, 2024, **24**(27), 8287–8295.

58 Y. Liu, Y. Song, Z. Zhu, C. Ji, J. Li, H. Jia, Y. Shi, F. Hu, Z. Zhao, D. Ding, B. Tang and G. Feng, Twisted-Planar Molecular Engineering with Sonication-Induced J-Aggregation To Design Near-Infrared J-Aggregates for Enhanced Phototherapy, *Angew. Chem., Int. Ed.*, 2024, **64**(7), e202419428.

59 L. Yuan, W. Lin, Y. Yang and H. Chen, A Unique Class of Near-Infrared Functional Fluorescent Dyes with Carboxylic-Acid-Modulated Fluorescence ON/OFF Switching: Rational Design, Synthesis, Optical Properties, Theoretical Calculations, and Applications for Fluorescence Imaging in Living Animals, *J. Am. Chem. Soc.*, 2012, **134**(2), 1200–1211.

60 Y. Tang, D. Xiang and Q. Li, In Situ Secondary Self-Assembly of Near-Infrared II J-Aggregates: A Novel Phototheranostic Strategy for Inducing Tumor Pyroptosis, *Adv. Mater.*, 2025, **37**, 2501184.

61 M. Cui, W. Li, Y. Chen, H. Liu, L. Liu, M. Ji and P. Wang, Aggregation-Enhanced Asymmetric Heptamethine Cyanine Nanoplatform for Imaging-Guided Synergistic Phototherapy and Ferroptosis, *Aggregate*, 2025, **6**, e70211.

62 C. Sun, B. Li, M. Zhao, S. Wang, Z. Lei, L. Lu, H. Zhang, L. Feng, C. Dou, D. Yin, H. Xu, Y. Cheng and F. Zhang, J-Aggregates of Cyanine Dye for NIR-II *in Vivo* Dynamic Vascular Imaging beyond 1500 nm, *J. Am. Chem. Soc.*, 2019, **141**, 19221–19225.

63 H. Li, H. Kim, F. Xu, J. Han, Q. Yao, J. Wang, K. Pu, X. Peng and J. Yoon, Activity-based NIR fluorescent probes based on the versatile hemicyanine scaffold: design strategy, biomedical applications, and outlook, *Chem. Soc. Rev.*, 2022, **51**(5), 1795–1835.

64 Q. Sun, D. He, L. Zhang, Z. Li, L. Qu and Y. Sun, Coumarin-hemicyanine-based far-red to near-infrared fluorescent probes: A new generation of fluorescent probe design platform, *TrAC, Trends Anal. Chem.*, 2023, **167**, 117272.

65 Z. Zeng, S. Liew, X. Wei and K. Pu, Hemicyanine-Based Near-Infrared Activatable Probes for Imaging and Diagnosis of Diseases, *Angew. Chem., Int. Ed.*, 2021, **60**(51), 26454–26475.

66 Y. Wei, X. Gao, J. Fang, Y. Xiao, J. Liu, Y. Liu, X. Zhang and B. Shen, Tailoring the pKa of Fluorescence Lifetime Imaging Probes to Visualize Aggrephagy and Resolve Its Microenvironmental Viscosity, *Anal. Chem.*, 2024, **96**(35), 14160–14167.

67 K. Wang, K. Gu, J. Cao, Y. Yang, H. Zhu, J. Shang and J. Zhou, Activatable Photoacoustic/Near-Infrared Probes for the Detection of Copper Ions of Cardiovascular Disease *in Vivo* and in Urine, *ACS Sens.*, 2024, **9**(9), 4898–4905.

68 Z. Chai, G. Pan, F. Qi, Y. Zhang, F. Dai, S. Zhang and B. Zhou, Cellular and Intravital ATP Imaging Using a Merocyanine-Hybrided Rhodamine Fluorescent Probe, *Anal. Chem.*, 2025, **97**(30), 16411–16420.

69 H. Pan, C. Wu, C. Lin, C. Hsu, Y. Tsai, P. Chowdhury, C. Wang, K. Chang, C. Yang, M. Liu, Y. Chen, S. Su, Y. Lee, H. Chiang, Y. Chan and P. Chou, Rational Design of Asymmetric Polymethines to Attain NIR(II) Bioimaging at >1100 nm, *J. Am. Chem. Soc.*, 2022, **145**(1), 516–526.

70 X. Zhang, Y. Chen, H. He, S. Wang, Z. Lei and F. Zhang, ROS/RNS and Base Dual Activatable Merocyanine-Based NIR-II Fluorescent Molecular Probe for *in Vivo* Biosensing, *Angew. Chem., Int. Ed.*, 2021, **60**(50), 26337–26341.

71 Z. Qin, T. B. Ren, H. Zhou, X. Zhang, L. He, Z. Li, X. B. Zhang and L. Yuan, NIRII-HDs: A Versatile Platform for Developing Activatable NIR-II Fluorogenic Probes for Reliable *in Vivo* Analyte Sensing, *Angew. Chem., Int. Ed.*, 2022, **134**(19), e202201541.

72 T. Ren, Z. Wang, Z. Xiang, P. Lu, H. Lai, L. Yuan, X. B. Zhang and W. Tan, A General Strategy for Development of Activatable NIR-II Fluorescent Probes for *in Vivo* High-Contrast Bioimaging, *Angew. Chem., Int. Ed.*, 2020, **60**(2), 800–805.

73 R. Acharya, S. Cekli, C. J. Zeman, R. M. Altamimi and K. S. Schanze, Effect of Selenium Substitution on Intersystem Crossing in π-Conjugated Donor-Acceptor-Donor Chromophores: The LUMO Matters the Most, *J. Phys. Chem. Lett.*, 2016, **7**(4), 693–697.

74 T. Weng, G. Baryshnikov, C. Deng, X. Li, B. Wu, H. Wu, H. Ågren, Q. Zou, T. Zeng and L. Zhu, A Fluorescence-Phosphorescence-Phosphorescence Triple-Channel Emission Strategy for Full-Color Luminescence, *Small*, 2020, **16**(7), 1906475.

75 B. Kim, H. Yeom, M. Yun, J. Kim and C. Yang, A Selenophene Analogue of PCDTBT: Selective Fine-Tuning of LUMO to Lower of the Bandgap for Efficient Polymer Solar Cells, *Macromolecules*, 2012, **45**(21), 8658–8664.

76 W. Lee, S. Son, K. Kim, S. Lee, W. Shin, S. Moon and I. Kang, Synthesis and Characterization of New Selenophene-Based Donor-Acceptor Low-Bandgap Polymers for Organic Photovoltaic Cells, *Macromolecules*, 2012, **45**(3), 1303–1312.

77 H. Saadeh, L. Lu, F. He, J. Bullock, W. Wang, B. Carsten and L. Yu, Polyselenopheno[3,4-b]selenophene for Highly Efficient Bulk Heterojunction Solar Cells, *ACS Macro Lett.*, 2012, **1**(3), 361–365.

78 Y. Wang, H. Masunaga, T. Hikima, H. Matsumoto, T. Mori and T. Michinobu, New Semiconducting Polymers Based on Benzobisthiadiazole Analogues: Tuning of Charge Polarity in Thin Film Transistors via Heteroatom Substitution, *Macromolecules*, 2015, **48**(12), 4012–4023.

79 N. James, Y. Chen, P. Joshi, T. Ohulchanskyy, M. Ethirajan, M. Henary, L. Strekowsk and R. Pandey, Evaluation of polymethine dyes as potential probes for near infrared fluorescence imaging of tumors: part - 1, *Theranostics*, 2013, **3**(9), 692–702.

80 R. Wang, M. He, Z. Zhang, T. Qiu, Y. Xi, X. Zeng, J. Fan, W. Sun and X. Peng, Photodynamic therapy promotes hypoxia-activated nitrogen mustard drug release, *Smart Mol.*, 2024, **2**(3), e20240010.

81 D. Ma, H. Bian, X. Zhang, K. Xin, Y. Yang, X. Peng and Y. Xiao, Tailored Engineering of Novel Xanthonium Polymethine Dyes for Synergetic PDT and PTT Triggered by 1064 nm Laser toward Deep-Seated Tumors, *Small*, 2021, **17**(21), 2100398.

82 C. Marian, Understanding and Controlling Intersystem Crossing in Molecules, *Annu. Rev. Phys. Chem.*, 2021, **72**, 617–640.

83 Y. Shimakura, THEORY OF INTERSYSTEM CROSSING IN AROMATIC COMPOUNDS: EXTENSION OF THE EL-SAYED RULE, *Chem. Phys.*, 1977, **19**, 155–163.

84 K. Lee, Y. Gao, W. Wei, J. Tan, Y. Wan, Z. Feng, Y. Zhang, Y. Liu, X. Zheng, C. Cao, H. Chen, P. Wang, S. Li, K. Wong and C. Lee, Anti-Quenching NIR-II J-Aggregates of Benzo[c]thiophene Fluorophore for Highly Efficient Bioimaging and Phototheranostics, *Adv. Mater.*, 2023, **35**(20), e2211632.

85 W. Chen, G. Luo and X. Zhang, Recent Advances in Subcellular Targeted Cancer Therapy Based on Functional Materials, *Adv. Mater.*, 2018, **31**(3), 1802725.

86 T. Pham, V. Nguyen, Y. Choi, S. Lee and J. Yoon, Recent Strategies to Develop Innovative Photosensitizers for Enhanced Photodynamic Therapy, *Chem. Rev.*, 2021, **121**(21), 13454–13619.

87 J. Ding, X. Zhao, S. Long, W. Sun, J. Du, J. Fan and X. Peng, A photoactivatable tumor-targeting in situ nanovaccine for large-volume tumor therapy, *Smart Mol.*, 2025, **3**(3), e70014.

88 J. Ding, Y. Lu, X. Zhao, S. Long, J. Du, W. Sun, J. Fan and X. Peng, Activating Iterative Revolutions of the Cancer-Immunity Cycle in Hypoxic Tumors with a Smart Nano-Regulator, *Adv. Mater.*, 2024, **36**(29), 2400196.

89 H. Jia, J. Liu, M. Shi, M. Abbas, R. Xing and X. Yan, Microneedle delivery systems for vaccines and immunotherapy, *Smart Mol.*, 2025, **3**(3), e20240067.

90 Z. Lin, T. He, M. Kang, W. Xie, D. Wang and B. Tang, The Fast-Growing Field of Cancer Immunotherapy Based on Aggregation-Induced Emission, *Aggregate*, 2025, **6**, e70189.

91 C. Zhang, X. Yin, L. Hao, Y. Wang, L. Dou, Q. Chen, J.-S. Lee, J. Wang, X. Peng, J. Yoon and H. Li, Integrin-Targeted, Activatable Nanophototherapeutics for Immune Modulation: Enhancing Photoimmunotherapy Efficacy in Prostate Cancer Through Macrophage Reprogramming, *Aggregate*, 2025, **6**, e70189.

92 CCDC 2431831: Experimental Crystal Structure Determination, 2026, DOI: 10.5517/ccdc.csd.cc2mmj5z.